

Seismic wavefield calculation for laterally heterogeneous whole earth models using the pseudospectral method

T. Furumura,* B. L. N. Kennett and M. Furumura†

Research School of Earth Sciences, Australian National University, Canberra ACT 0200, Australia

Accepted 1998 June 18. Received 1998 May 11; in original form 1998 January 5

SUMMARY

A method for simulating seismic wave propagation in a laterally heterogeneous whole earth model is presented by solving the elastodynamic equations in 2-D cylindrical coordinates using the pseudospectral method (PSM). The PSM is an attractive time-domain technique that uses the fast Fourier transform for an accurate differentiation of field variables in the equations. Since no dispersion error arises in Fourier differentiation, even when using a large grid spacing, computer memory and time are reduced by several orders of magnitude compared to traditional finite-difference methods. In order to examine body-wave phases with current computing resources, a slice through the sphere is approximated with a 2-D cylindrical model. An irregular grid spacing is used in the vertical coordinate to improve the treatment of the various structural boundaries appearing in the earth model by matching the heterogeneity in the model. Synthetic seismograms obtained by the PSM calculation are compared with those calculated from an exact simulation method for a spherically homogeneous (1-D) earth model and achieve good agreement.

The PSM method is illustrated by constructing the seismic P – SV wavefield for strongly heterogeneous earth models including a shield structure near the free surface and velocity perturbations just above the core–mantle boundary. The visualization of the evolution of seismic P and S waves in time and space is tracked using a sequence of snapshots and synthetic seismograms. These displays allow direct insight into the nature of the complex seismic wave behaviour in the Earth's interior.

Key words: core–mantle boundary, finite-difference method, pseudospectral method, seismic modelling, wave propagation, whole earth.

1 INTRODUCTION

A number of studies have recently been conducted with the object of simulating seismic wave propagation in spherical earth models in order to complement the results obtained from observed broad-band records. For example, Wysession & Shore (1994) simulated seismic SH waves in the mantle using a modal summation technique and Cummins *et al.* (1994a,b) used the Direct Solution Method for the seismic wave simulation of a spherically symmetric earth model. Friederich & Dalkolmo (1995) calculated complete synthetic seismograms using a numerical integration technique. For spherically heterogeneous earth models, such as have been derived from high-resolution tomography studies, the requirements for wavefield modelling are more severe. In this heterogeneous

case, in which material parameters may vary with both angular and vertical direction independently, simulation techniques have recently been extended by solving the elastodynamic equations with finite-difference approximations (e.g. Alterman *et al.* 1970; Igel & Weber 1995, 1996; Yoon & McMechan 1995; Chaljub & Tarantola 1997; Igel & Gudmundsson 1997) and by exploiting Galerkin weak-form expansions (Cummins *et al.* 1997). For large-scale seismic wave propagation in a whole earth model, strong material discontinuities need to be taken into account in the mantle. Much effort has been expended to achieve accurate results with reduced computational requirements, since numerical errors such as grid dispersion in traditional finite-difference schemes usually distort the pulse shape propagated for longer distances unless a very small grid spacing is employed and/or higher-order finite-difference approximations are used (see e.g. Fornberg 1987).

The pseudospectral method (e.g. Kosloff *et al.* 1984) we use here is an attractive alternative to the traditional finite-difference scheme that uses an accurate differentiation scheme using the fast Fourier transform (FFT) for calculating

* Present address: Hokkaido University of Education, Midorigaoka 2-34-1, Iwamizawa, 068, Japan.

† Present address: Hokkaido University, Kita-ku, N10 W8, Sapporo, 060, Japan.

the spatial derivatives in the equations; therefore accurate results can be obtained even with large grid spacing so that computational memory and time are considerably reduced compared to the traditional finite-difference simulations (see e.g. Fornberg 1987; Daut *et al.* 1989; Vidale 1990). For this reason the PSM modelling has typically been applied for large-scale and high-frequency seismic wave modelling in both 2-D (e.g. Kang & McMechan 1990; Furumura & Takenaka 1996) and 3-D models (e.g. Reshef *et al.* 1998; Furumura *et al.* 1998) using the Cartesian coordinate system.

Here we present the PSM simulation for the modelling of seismic P and SV waves in a 2-D heterogeneous earth structure. We simplify the problem by considering a slice through the sphere and solve the elastodynamic equations in a 2-D cylindrical coordinate system rather than in spherical coordinates. This approximation enables us to produce results for comparatively high-frequency body waves (periods up to 15 s propagating for the whole 360° range of the earth) within the limitation of current computer resources. There is the further advantage of avoiding the pole axis at $\varphi=0, \pi$ in the full spherical coordinate system, which cannot be simply treated in the numerical simulation of a 360° earth model. For simple configurations we expect that the major difference in the wavefields obtained from the 2-D approximation and the full spherical simulations will arise from the geometrical spreading factors and the configuration of seismic sources implicitly assumed in these coordinate systems. In 2-D cylindrical coordinates we will have a symmetric line source, whereas in the 2-D spherical coordinates we would use an axisymmetric ring source.

The application of the PSM to the solution of wave propagation problems in 2-D cylindrical or polar coordinate systems has already been conducted for the forward modelling of geophysical exploration experiments for boreholes (Kessler & Kosloff 1990, 1991; Tessmer *et al.* 1992) and around circular objects such as a cavity. These treatments used Chebyshev polynomials for the expansion of field variables in the vertical direction, rather than using the Fourier transform, since an accurate representation of the free surface and the rigid boundary conditions can be naturally incorporated in the Chebyshev transform at the edge of the domain. However, the Chebyshev transform is defined through a set of special collocation points with decreasing grid intervals towards boundaries, which leads to severe stability problems and the need for a very small time step. In order to avoid this problem, Kosloff *et al.* (1990) used a coordinate transform to recast the Chebyshev mesh in order to enlarge grid intervals, and Kessler & Kosloff (1991) developed a multidomain technique by combining a set of concentric regions, each with a separate Chebyshev mesh associated with suitable boundary conditions to combine the subregions. Therefore, the design of a Chebyshev mesh that is suitable for both computational requirements and the representation of the structural heterogeneity in a whole earth model would be rather difficult.

In this paper we use the pseudospectral method with a Fourier transform in both vertical and angular directions with the use of an irregularly arranged grid model using a mapping technique (Fornberg 1988) in the vertical direction. We make use of the irregular grid model so the spatial resolution in this coordinate is improved and therefore structural heterogeneity in the earth model can be adequately treated even using a coarse PSM grid.

In the following sections we first give an explanation of the PSM scheme for calculating seismic P – SV -wave propagation in the 360° earth using the 2-D cylindrical coordinate system. In order to demonstrate the effectiveness of the modelling procedure we will conduct a series of simulations of 2-D wavefields in a laterally homogeneous earth model. We compare the simulation result with that obtained from an exact method to show the accuracy of the PSM simulation. We then evaluate the wavefield in models with strongly heterogeneous inclusions in the uppermost mantle or just above the core–mantle boundary. The behaviour of the wavefield will be illustrated by using a sequence of wavefield snapshots derived directly from the time-domain simulation for each model, together with synthetic seismograms at surface stations at regular intervals around the Earth's circumference. The combination of this information helps to provide a direct insight into the nature of seismic wave behaviour in the different classes of models of the Earth's interior.

2 2-D PSM MODELLING OF P – SV WAVES IN A CYLINDRICAL COORDINATE SYSTEM

2.1 Equation of motion in a 2-D cylindrical coordinate system

We will consider a 2-D cylindrical coordinate system with coordinates (r, θ, z) , where all fields are invariant in z (i.e. $\partial/\partial z=0$). The equations of momentum conservation for the 2-D wavefield are then (Aki & Richards 1980; Fung 1965)

$$\rho \ddot{U}_r = \frac{1}{r} \frac{\partial}{\partial r} (r \sigma_{rr}) + \frac{1}{r} \frac{\partial \sigma_{r\theta}}{\partial \theta} - \frac{\partial \sigma_{\theta\theta}}{r} + f_r$$

and

$$\rho \ddot{U}_\theta = \frac{1}{r^2} \frac{\partial}{\partial r} (r^2 \sigma_{r\theta}) + \frac{1}{r} \frac{\partial \sigma_{\theta\theta}}{\partial \theta} + f_\theta, \quad (1)$$

where $\ddot{U}_p = \ddot{U}_p(r, \theta, t)$ ($p=r, \theta$) are the acceleration in the vertical r and angular θ directions at a gridpoint (r, θ) at time t , $\rho = \rho(r, \theta)$ is the mass density, $f_p = f_p(r, \theta, t)$ ($p=r, \theta$) are body forces and $\sigma_{pq} = \sigma_{pq}(r, \theta, t)$ ($p, q=r, \theta$) are the stress components,

$$\sigma_{rr} = (\lambda + 2\mu) \frac{\partial U_r}{\partial r} + \frac{\lambda}{r} \frac{\partial U_\theta}{\partial \theta} + \frac{\lambda}{r} U_r,$$

$$\sigma_{\theta\theta} = \lambda \frac{\partial U_r}{\partial r} + \left(\frac{\lambda + 2\mu}{r} \right) \frac{\partial U_\theta}{\partial \theta} + \left(\frac{\lambda + 2\mu}{r} \right) U_r,$$

$$\sigma_{r\theta} = \frac{\mu}{r} \frac{\partial U_r}{\partial \theta} + \mu \frac{\partial U_\theta}{\partial r} - \frac{\mu}{r} U_\theta, \quad (2)$$

where $U_p = U_p(r, \theta, t)$ ($p=r, \theta$) are the displacement components, $\lambda = \lambda(r, \theta)$ is the Lamé modulus and $\mu = \mu(r, \theta)$ is the shear modulus. The seismic source for a double-couple line source can be incorporated into these equations by using an equivalent body force (see e.g. Aki & Richards 1980, Chapter 3).

2.2 Seismic source

The body force for a double-couple line source corresponding to a set of moment rate tensor components $M_{rr}(t)$, $M_{r\theta}(t)$, and

$M_{\theta\theta}(t)$ can be written as

$$\begin{aligned} f_r(r, \theta, t) &= -M_{rr}(t) \frac{\partial}{\partial r} \hat{\sigma}(r-r_0, \theta-\theta_0, t-t_0) \\ &\quad - M_{r\theta}(t) \frac{\partial}{\partial \theta} \hat{\sigma}(r-r_0, \theta-\theta_0, t-t_0), \\ f_\theta(r, \theta, t) &= -M_{r\theta}(t) \frac{\partial}{\partial r} \hat{\sigma}(r-r_0, \theta-\theta_0, t-t_0) \\ &\quad - M_{\theta\theta}(t) \frac{\partial}{\partial \theta} \hat{\sigma}(r-r_0, \theta-\theta_0, t-t_0), \end{aligned} \quad (3)$$

where $\hat{\sigma}$ is a pseudo-delta function introduced into the discrete grid over a small region and time around the centre of the source (r_0, θ_0) at time t_0 , and

$$\hat{\sigma}(r, \theta, t) = \bar{\sigma}_s(r) \bar{\sigma}_s(\theta) \bar{\sigma}_t(t), \quad (4)$$

where $\bar{\sigma}_s$ and $\bar{\sigma}_t$ are Herrmann's pseudo-delta functions (Herrmann 1979). $\bar{\sigma}_s$ extends over some gridpoints in space and $\bar{\sigma}_t$ covers the source time duration. We use the pseudo-delta source distribution in space rather than a strict point source (i.e. Dirac delta function) because spatial differentiation calculation using an FFT with finite wavenumbers often produces an aliasing error around the discontinuity in the wavefield from a point source that leads to instability in the calculation (see e.g. Kosloff *et al.* 1984; Furumura & Takenaka 1992).

2.3 Time integration

The displacements at the next time step are explicitly evaluated from the wavefield at the current and previous time steps. For example, the following second-order finite-difference scheme is often used:

$$\dot{U}_p[r, \theta, (n+1/2)\Delta t] = \dot{U}_p[r, \theta, (n-1/2)\Delta t] + \ddot{U}_p[r, \theta, n\Delta t]\Delta t \quad (5)$$

and

$$U_p[r, \theta, (n+1)\Delta t] = U_p[r, \theta, (n-1)\Delta t] + \dot{U}_p[r, \theta, (n+1/2)\Delta t]\Delta t, \quad (6)$$

where $\dot{U}_p = \dot{U}_p(r, \theta, t)$ ($p=r, \theta$) denotes the particle velocity and Δt is the time step, which is constrained by the ratio of minimum grid spacing, Δ^{\min} , in the numerical mesh to maximum wave-propagation speed, V^{\max} , so that

$$\Delta t < \alpha \frac{\Delta^{\min}}{V^{\max}}, \quad (7)$$

where α is a coefficient that defines the accuracy in the time integration calculations in order to minimize the error below an acceptable level [e.g. $\alpha=0.26$ for a 1 per cent tolerance error level for the second-order approximation; see Daudt *et al.* (1989)].

High-accuracy integration schemes such as those based on higher-order Taylor's expansions (e.g. Igel & Weber 1995), the Runge-Kutta method (e.g. Kosloff *et al.* 1990) and spectral integration techniques using Chebyshev expansions (Tal-Ezer *et al.* 1990) could also be applied in the integration scheme and lead to a larger value of α (i.e. larger allowed Δt), but at the cost of additional computational memory and time.

2.4 Anelastic attenuation

Anelastic attenuation in the medium is simply incorporated in the time-domain simulation by multiplying the values at each gridpoint of the stress and velocity field by the attenuation coefficients given by Graves (1996) as

$$A(r, \theta) = \exp[-\pi f_0 \Delta t / Q(r, \theta)], \quad (8)$$

where Q is the anelastic attenuation factor for a reference frequency f_0 . This form implies a frequency-dependent quality factor of the form $Q(f) = fQ_0/f_0$, where Q_0 is the quality factor at the reference frequency (see Graves 1996). This convenient attenuation scheme requires little computational memory and time and it is therefore very efficient for the implementation of large-scale simulations. However, a significant drawback is that a separate allowance cannot be made for the anelastic attenuation of compressional (P) and shear (S) waves. We therefore use an averaged attenuation factor of Q_P and Q_S , $Q^{-1} = (Q_P^{-1} + Q_S^{-1})/2$, and the reference frequency f_0 for the dominant source frequency, so both the P and the S wavefields should be moderately attenuated.

2.5 Boundary condition

Boundary conditions for the displacement and stress components at the internal interfaces in the simulation model are implicitly treated in the PSM modelling by changes in the elastic parameters and density that are assigned at each gridpoint.

The free-surface boundary condition at the Earth's surface is simply incorporated into the calculation by introducing an air-filled zone with $\lambda=\mu=0$ over the surface, while the density ρ keeps the value just below the surface to preserve computational stability at the free surface (see Graves 1996). The periodicity of the FFT will also lead to a free-surface boundary at the base of the model in the Earth's interior; an absorbing boundary with a 20-grid buffer zone following Cerjan *et al.* (1985) is applied at the bottom to reduce artificial reflections. The periodic boundary condition in the angular direction for the whole earth modelling is naturally incorporated in the calculation from the periodicity in the FFT.

2.6 Angular spatial differentiation ($\partial/\partial\theta$) by using the FFT

In the PSM the spatial derivatives in eqs (1) and (2) are analytically calculated in the wavenumber domain, and the transformation between the physical domain and the wavenumber domain is efficiently performed by means of an FFT as follows. First the field quantity $f(n\Delta\theta)$ ($n=0, 1, \dots, N-1$) at spatially discrete locations with a uniform interval of $\Delta\theta$ at a given depth r is transformed into the wavenumber domain by the 1-D FFT,

$$F(l\Delta k) = \Delta\theta \sum_{n=0}^{N-1} f(n\Delta\theta) e^{-i2\pi nl/N}, \quad (9)$$

where

$$F(l\Delta k) [l=0, 1, \dots, N-1; \Delta k = 2\pi/(N\Delta\theta)]$$

represents the Fourier transform of $f(n\Delta\theta)$. The data are then multiplied by the imaginary unit i and spatial wavenumber $l\Delta k$ to achieve the differentiation. They are then transformed back into the physical domain using an inverse FFT,

$$\frac{d}{d\theta} f(n\Delta\theta) = \frac{1}{N\Delta\theta} \sum_{l=0}^{N-1} i(l\Delta k)F(l\Delta k)e^{i2\pi nl/N}. \quad (10)$$

For the differentiation of 2-D variables, the calculation of (9) and (10) is carried out sequentially along the r direction. Since the Fourier differentiation gives exact results up to the Nyquist wavenumber ($k_N = 2/N\Delta k$), as few as two grid-points per minimum wavelength are theoretically sufficient for treating seismic waves in the PSM simulation. This is a major attraction of the PSM compared with the traditional lower-order finite-difference method which needs much smaller grid spacing for simulating seismic wave propagation without developing large grid dispersion.

2.7 Vertical spatial differentiation ($\partial/\partial r$) for an irregular grid configuration

We use an irregular grid configuration in the vertical coordinate (r) in order to improve the spatial resolution in this direction and to include structural discontinuities in the coarse PSM grid. In the angular (θ) direction a uniform grid spacing is used, since the scale of heterogeneity in this direction is relatively large compared to the vertical direction.

Fig. 1 illustrates the PSM grid configuration for the seismic wave simulation in an earth model. In this model the grid size in the vertical direction (Δr) is chosen to be small at the free surface and the CMB, where strong heterogeneity exists, and is gradually enlarged as the distance from the boundaries increases. This grid configuration with a number of grid-points in the vicinity of large material discontinuities such as just below the free surface and around the CMB is, at the same time, quite efficient in suppressing the Gibbs's noise produced during the differentiation calculation using the FFT at the discontinuities, since this oscillation noise decays exponentially as the number of gridpoints from the boundary increases.

To calculate the derivatives of unequally arranged data, we use a mapping technique introduced by Fornberg (1988) for evaluating the derivatives using an ordinal FFT for equally sampled data. The differentiation in the vertical r direction in eqs (1) and (2) is calculated as follows. First the derivatives are evaluated using the ordinary differentiation scheme assuming a regular grid interval of Δr_0 and a corresponding discrete wavenumber of $\Delta k_0 = 2\pi/N\Delta r_0$ as

$$\frac{d}{d\xi} f(n\Delta r_0) = \frac{1}{N\Delta r_0} \sum_{l=0}^{N-1} i(l\Delta k_0)F(l\Delta k_0)e^{i2\pi nl/N}. \quad (11)$$

The results are then multiplied by compensation factors, which are defined by the ratio of the actual grid size at each point $\Delta r(r)$ to the assumed regular grid size Δr_0 , and the derivative at

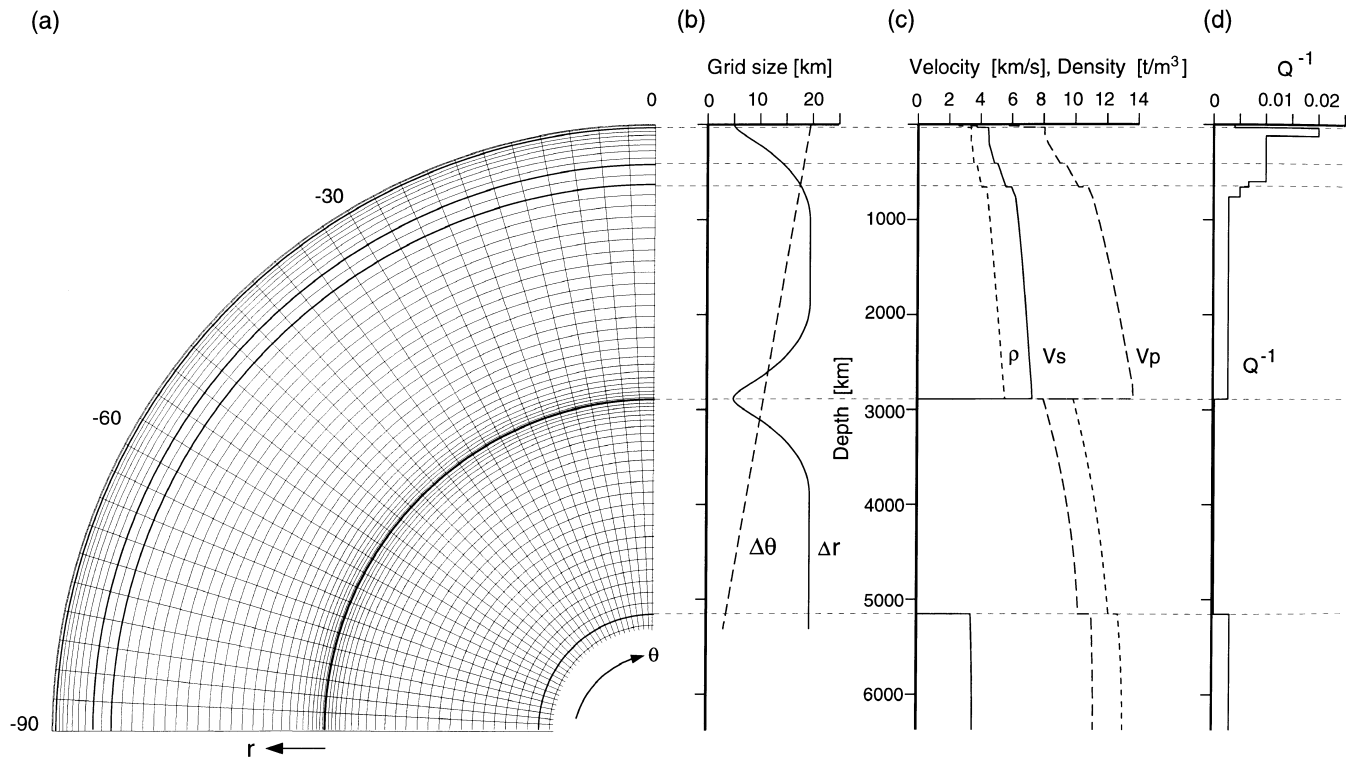


Figure 1. Grid configuration and structure for the whole earth model. (a) Grid configuration of the vertical (r) and angular (θ) directions. Only a quarter-space in the whole Earth is displayed. Air zone over the free surface is not displayed in the figure. (b) Grid size as a function of depth. (c) P - and S -wave velocity structure in the spherically symmetric IASP91 earth model (Kennett & Engdahl 1991) and the density (ρ) based on the PREM model (Dziewonski & Anderson 1981). (d) Anelastic attenuation coefficient (Q^{-1}).

each gridpoint is evaluated by the chain rule as

$$\begin{aligned} \frac{d}{dr} f(n\Delta r) &= \frac{d\xi}{dr} \frac{d}{d\xi} f(n\Delta r_0) \\ &= \frac{\Delta r_0}{\Delta r(r)} \frac{d}{d\xi} f(n\Delta r_0). \end{aligned} \quad (12)$$

Complete details of the mapping technique for the application of PSM calculation, demonstrating the accuracy of the differentiation and introducing the application of irregular grid models such as for accurate incorporation of curved interfaces and surface topography, can be found in e.g. Fornberg (1988), Tessmer *et al.* (1992) and Nielsen *et al.* (1994).

3 SIMULATION OF SEISMIC WAVES IN LATERALLY HOMOGENEOUS AND HETEROGENEOUS EARTH MODELS

In order to demonstrate the feasibility of the PSM for large-scale Earth simulation we have conducted a sequence of seismic wave simulations using both a spherically symmetric earth model and a model with strong localized heterogeneity.

In this section we first discuss the propagation of seismic waves from a deep (600 km) source in a spherically symmetric earth. This enables us to identify the phases generated at the free surface and internal interfaces and their subsequent propagation in the mantle and core. We compare synthetic seismograms calculated by the PSM simulation with an exact waveform obtained by a DSM calculation (Cummins *et al.* 1994b) to show the accuracy of the PSM.

We look at the influence of regions of significant heterogeneity (± 5 per cent perturbation) placed just below the free surface and just above the CMB on the character of the seismic wavefield. The zones with the strongest recognized heterogeneity in the mantle lie in the upper 400 km or in the D'' zone just above the CMB. By comparing the results for the heterogeneous models with the spherically symmetric reference earth model we can isolate the influence of the heterogeneity and examine the way in which the presence of different classes of heterogeneity modifies the seismic wavefield.

3.1 Example 1: spherically symmetric earth

The whole earth model we use here is based on the seismic velocities from the spherically homogeneous IASP91 model (Kennett & Engdahl 1991), supplemented with density and anelastic attenuation structure based on the PREM model (Dziewonski & Anderson 1981), with adjustments in the upper-mantle structure to match the absence of a 210 km discontinuity in IASP91. The representation of the model employs 2048 nodes in the angular direction with a regular grid interval of $\Delta\theta = 0.1758^\circ$ to cover the full angular range of 360° . The spacing of the vertical gridpoints on surfaces of constant radius, in the circular coordinate model, ranges from $\Delta r = 19.5$ km at the free surface to 5 km at the base of the grid in the inner core. In the vertical direction 512 nodes are used, extending from 735 km above the free surface in the air zone to 5315 km below the surface, including the whole of the mantle and the outer core. Note that because of the singularity in the cylindrical coordinate system at the centre of the earth ($r=0$), the inner-core zone is excluded from the numerical model.

Using the minimum S -wave velocity just below the surface ($V_S = 3.36$ km s $^{-1}$) and the minimum S wavelength (50.4 km) for a source with a dominant period of 15 s, the number of gridpoints per wavelength for this model is 2.58, which is sufficient for the PSM simulation. A time step of $\Delta t = 0.1$ s is used, which is derived from the minimum grid size (5 km) and maximum wave-propagation speed ($V_P = 13.7$ km s $^{-1}$) around the CMB.

We use a double-couple line source for a strike-slip fault model placed on a node at 600 km depth, which imparts seismic waves with a Herrmann pseudo-delta function (Herrmann 1979) source time history with a dominant period around 15 s. The deep (600 km) source has been chosen so that P and SV waves are radiated directly into the mantle with a clear separation from the depth phases produced from the reflection of the direct waves at the free surface.

3.1.1 Wavefield snapshots

We illustrate the propagation characteristics for the P - SV seismic wavefield in the spherically symmetric earth model by a sequence of snapshots (Fig. 2). A regular time interval of 120 s between frames is employed from initiation of the P - and S -wave radiation from the source until the core phase PKP approaches the free surface (1080 s frame). We also display some other frames at later times (1320, 1680 and 2280 s), which display further features of interest. In order to enable a ready interpretation of the wavefield each snapshot represents the P - and SV -wave contributions constructed from the divergence and curl of the wavefield:

$$\begin{aligned} P: & \left| \frac{1}{r} \frac{\partial(rU_r)}{\partial r} + \frac{1}{r} \frac{\partial U_\theta}{\partial \theta} \right|, \\ SV: & \left| \frac{1}{r} \frac{\partial(rU_\theta)}{\partial r} - \frac{1}{r} \frac{\partial U_r}{\partial \theta} \right|. \end{aligned} \quad (13)$$

The P -wave contribution is shown in red and the SV -wave component in green.

The sequence of snapshots provides an effective summary of the propagation of the major seismic phases. In the first frame (120 s) of Fig. 2 we see the P and S waves radiating from the double-couple source, with a near-circular wave front modulated by four-lobe radiation patterns. The shapes of the wave fronts are slightly distorted from a circle because of the influence of the 410 and 660 km discontinuities. The P wave radiating upwards from the source has been reflected at the free surface and propagates back into the mantle as a pP phase. We can also see small P and S reflections from the upper-mantle discontinuity at 410 km; reflections from the 660 km discontinuity are not visible because the source depth (600 km) lies so close to the interface.

In the 240 s frame we see strong surface reflected phases sS and sP generated from upgoing S . The free-surface conversion pS with propagation close to vertical is separating from the P -wave front. The main P -wave front has reached the CMB, with transmission in the core PK with a flattened wave front induced by the significant drop in the P -wave velocity and the consequent sharp refraction towards the vertical. The core PcP and PcS reflections from the CMB propagate back into the mantle.

At the 360 s frame the pP phase front has reached the CMB, producing $pPcP$ and $pPcS$ reflections and a pPK transmitted

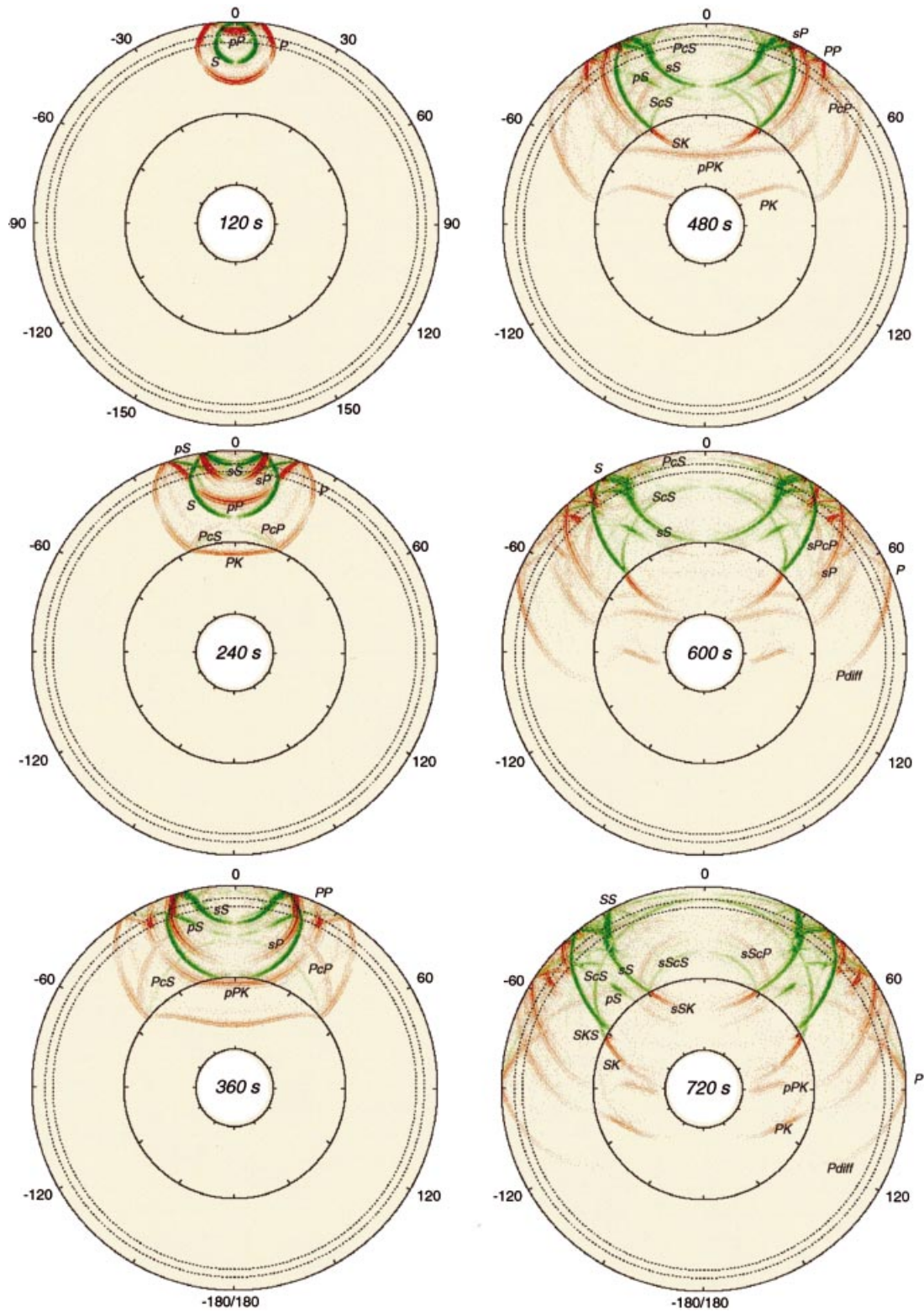


Figure 2. Snapshots of seismic waves from a 600 km deep source propagating in a spherically symmetric earth model. The *P*-wave contribution is shown in red and the *SV*-wave contribution in green. The discontinuities at 410 and 660 km are indicated by dotted lines, and boundaries at the CMB and inner-core/outer-core boundary (ICB) are shown as solid lines. The elapsed time from the source initiation is shown in the middle of each frame. The major seismic *P* and *S* phases are labelled in the right and left hemispheres, respectively.

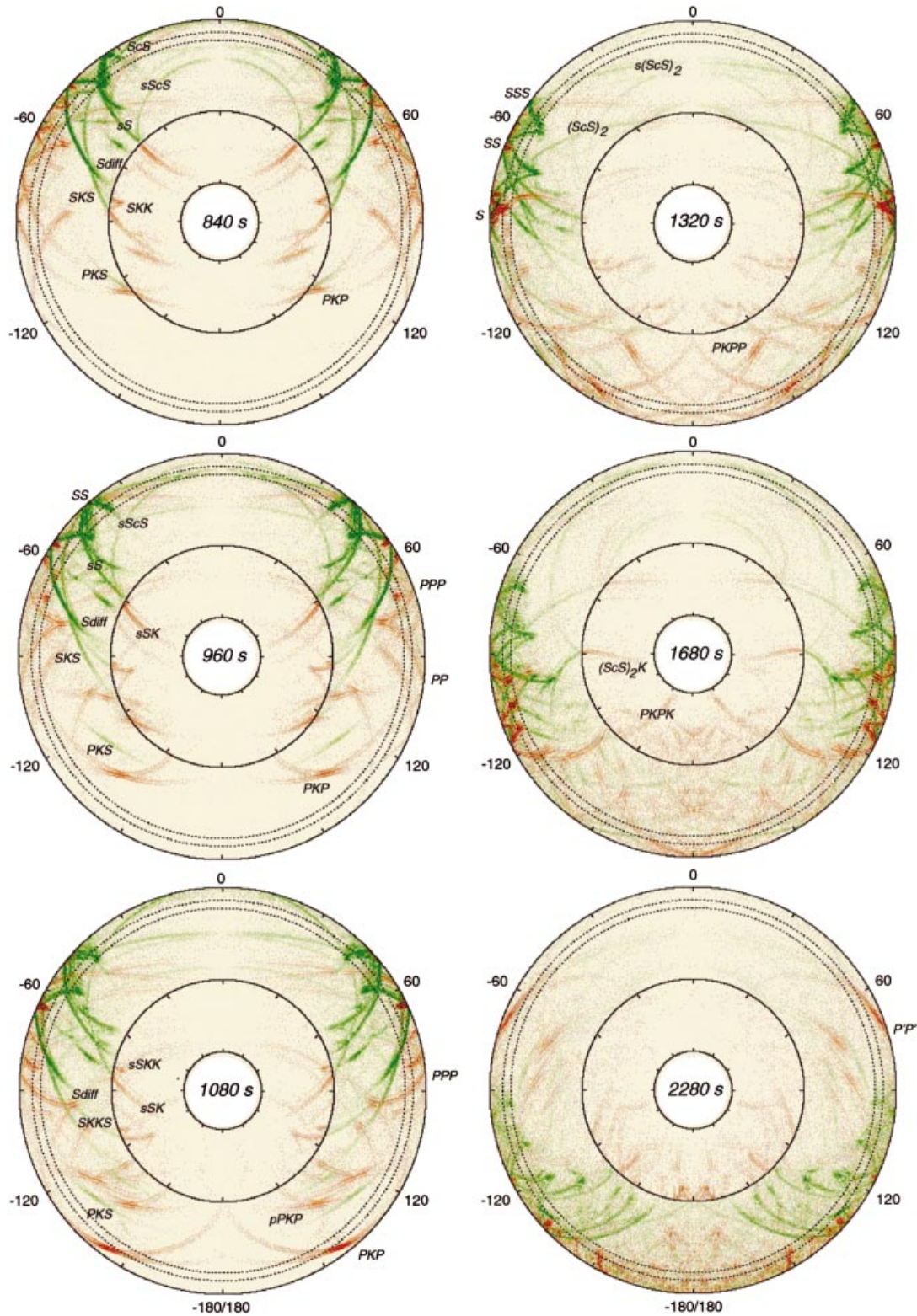


Figure 2. (Continued.)

wave. Multiple *P* reflections (*PP*) are superposed on *pP*, producing large energy between the upper-mantle discontinuities at 410 and 660 km. The *PcP* phase approaches the free surface and the *PcS* phase is clearly seen in the lower mantle. The *S*-wave front has just impinged on the CMB. By the

480 s frame the *PP* phase is a prominent feature in the uppermost mantle at a distance of around 40° linking with *P*-to-*S* conversions at the free surface. A strong converted phase *SK* has been produced in the core from the incident *S*-wave front since no shear wave can exist in the liquid

core. The *ScS* reflection from the CMB is visible, but the *ScP* conversion is too small to be discerned in the snapshot. In the 600 s frame there is a clear separation between the *P*-, *S*- and *sS*-wave fronts. The different classes of core reflection such as the *PcS* and *sPcP* successively approaching the free surface in the region close to the epicentre.

By 720 s the *P* wave has almost reached an epicentral distance of 90° at the surface and merged with the *PcP* arrival. For distances greater than 100° the first *P* arrival to reach the surface is a diffracted *P_{diff}* phase propagating through the lower mantle, which is just discernible at the tip of the *P*-wave front in the 600 and 720 s frames. The multiple *S* phases in the upper mantle produce large amplitudes at the free surface around 30°. Because the compressional velocity in the core is faster than the shear velocity at the base of the mantle, the *SK* phase propagating in the core has a slightly faster propagation speed than the *S*-wave speed in the lowermost mantle, and as a consequence the *SK*-wave front connected with the *ScS*-wave front in the mantle (480 s) gradually separates from the *S*-wave front in the lowermost mantle. This produces a triplication between these *S*-wave groups with a complex wave-front pattern. In the 840 s frame there is a clear separation of an *SKS* phase propagating back into the mantle, while internal reflection at the CMB produces an *SKK* phase in the core. On the far side of the core the *PK* phase impinges on the CMB with a large incidence angle and produces the mantle phases *PKP* and *PKS* in transmission.

At 960 s multiple *PP* and *PPP* reverberations in the mantle have developed, showing an obvious 'Y'-shaped wave front. Such a feature associated with free-surface multiples is also found between the *S* and *SS* waves. The group of arrivals associated with *sS* produces another *S*-wave triplication between the *sS*, *sSK* and *sScS* phases just above the CMB. In

the 1080 s frame the *PKP* approaches the free surface with a large amplitude at an epicentral distance around 144° as the various branches of the *PKP*-wave front coalesce after having taken somewhat different paths.

In the later frames we isolate a number of different wave-propagation phenomena. At 1320 s the multiple reflections of the free surface and the CMB such as (*ScS*)₂ and *s*(*ScS*)₂ are clearly seen. *S* itself approaches 100° at the surface, and is followed by a complex train of surface multiples such as *SS* and *SSS*. The *PKP* phase reflected at the surface propagates back through the mantle and penetrates the core (see the 1680 s frame); it finally returns to the surface as the *P'P'* [i.e. (*PKP*)₂] phase, which is typically observed with a focusing near 284° from the epicentre (see around 76° on the 2280 s frame).

3.1.2 Synthetic seismograms

The snapshots give a clear depiction of the internal processes that lead to the surface seismograms displayed in Fig. 3. Record sections of synthetic velocity seismograms for both the vertical and the angular components are presented together with key diagrams showing the arrival times for major body-wave phases for the IASP91 model. *P* phases are displayed with the vertical component and *S* phases with the angular component. These ray-theoretical times are also superposed on the synthetic seismograms, showing good agreement with the numerical modelling.

At epicentral distances below 100°, the first arrival is the direct *P* wave propagating through the mantle from the source, which has a large amplitude at a distance of around 80° with the superposition of the *PcP* phase. While the first *P* arrivals beyond 100° are small, the *P_{diff}* phase can be discerned in the seismograms to at least a distance of 120°. Multiple *P*

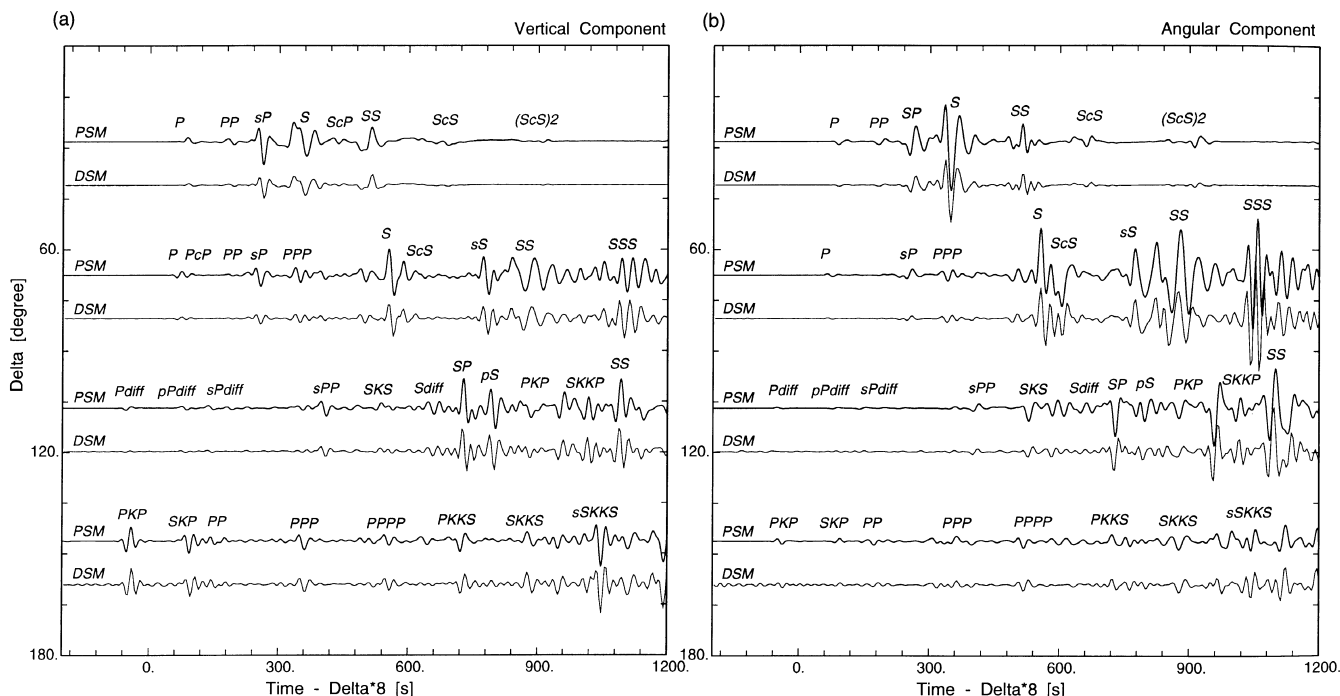


Figure 4. Comparison of PSM (thick lines) and DSM (thin lines) synthetic seismograms for the IASP91 spherically symmetric earth model at four different epicentral distances. Each trace is normalized by a compensation factor for the seismic geometrical spreading of the line source (PSM) and the point source (DSM) to recover the wave amplitude at larger distances. Major phases are marked.

reflections at the free surface such as *PP*, *PPP* and *PPPP* are clearly seen in the seismograms with large amplitudes around 40° , 60° and 80° from the epicentre. The *S*-wave multiples such as *SS* and *SSS* are found in broad distance ranges with large and long wave trains on both vertical and angular components. Triplications between the direct *S*, *ScS*–*SKS* and *S_{diff}* phases and between the *sS*, *sScS*–*sSKS* and *sS_{diff}* phases are obvious at epicentral distances around 80° and 84° , respectively. As expected, we see a clear separation between the *PKP* phase on the vertical component and converted core phase *SKS* and the core reflection *ScS* phase on the angular component.

3.1.3 Comparison of synthetic seismograms with another method

In order to demonstrate the accuracy of the PSM simulation, we compare the synthetic seismograms with that derived from another simulation scheme, the Direct Solution Method (DSM: Geller & Ohminato 1994; Cummins *et al.* 1994), which gives an exact waveform for spherically symmetric media. The seismic source and the structural model used are the same as those illustrated in the previous section, including both mantle and core but just a radial variation in seismic properties. Anelastic attenuation (Q) was excluded, since the treatment of anelasticity in the two schemes is completely different. We applied low-pass filtering with a cut-off period of $T=15$ s in order to reduce the numerical noise that arose during the calculation using the infinite- Q structural model in the simulation. Fig. 4 compares the synthetic velocity seismograms of the vertical and angular components of displacement calculated using both the PSM and the DSM for distances close to 30° , 70° , 110° and 150° from the epicentre. The traces for the two methods are calculated at the same distance but are displaced in the displays for ease of comparison. The geometrical spreading from the line double-couple source for the 2-D wavefield in 2-D cylindrical coordinates in the PSM method and the point double-couple used in the DSM approach in spherical coordinates are somewhat different. However, in the far field we can make a compensation for the differences by multiplying the PSM seismograms by a factor of $R^{-0.5}$, where R is the distance from the epicentre, to give the corrected amplitude of the waveform for a point source. In Fig. 4 there is good agreement between the seismograms calculated using the two different methods at every epicentral distance, demonstrating the accuracy in the PSM calculation including source implementation and boundary conditions. Some differences in the wave shape, especially at later times and larger distances such as are obviously seen in the *SS* and *SSS* phases (e.g. see the seismogram at 70°) are likely to be mainly due to the simplicity of the geometrical spreading correction for arrivals with very different paths, the difference in the pulse shape between a point and a line source in far-field waveforms (see e.g. Vidale *et al.* 1985; Song & Williamson 1995; Furumura & Takenaka 1996) and subtle differences in the discretization of the velocity structure represented by a coarse PSM grid.

3.2 Example 2: uppermost mantle heterogeneity

We now consider the introduction of large-scale heterogeneity in the uppermost mantle and look at the way in which such features modify the character of the wavefield. The model

consists of a +5 per cent anomaly zone (with faster V_P , V_S and larger ρ , Q than the reference model) with a trapezoidal shape 2500 km long by 250 km deep, which is emplaced below the free surface in the distance range $\pm 30^\circ$ to $\pm 55^\circ$ from the source. The anomaly is a representation of a shield structure such as the craton of the Australian continent, but the anomaly scale we employ here is slightly larger than reality (e.g. Zielhuis

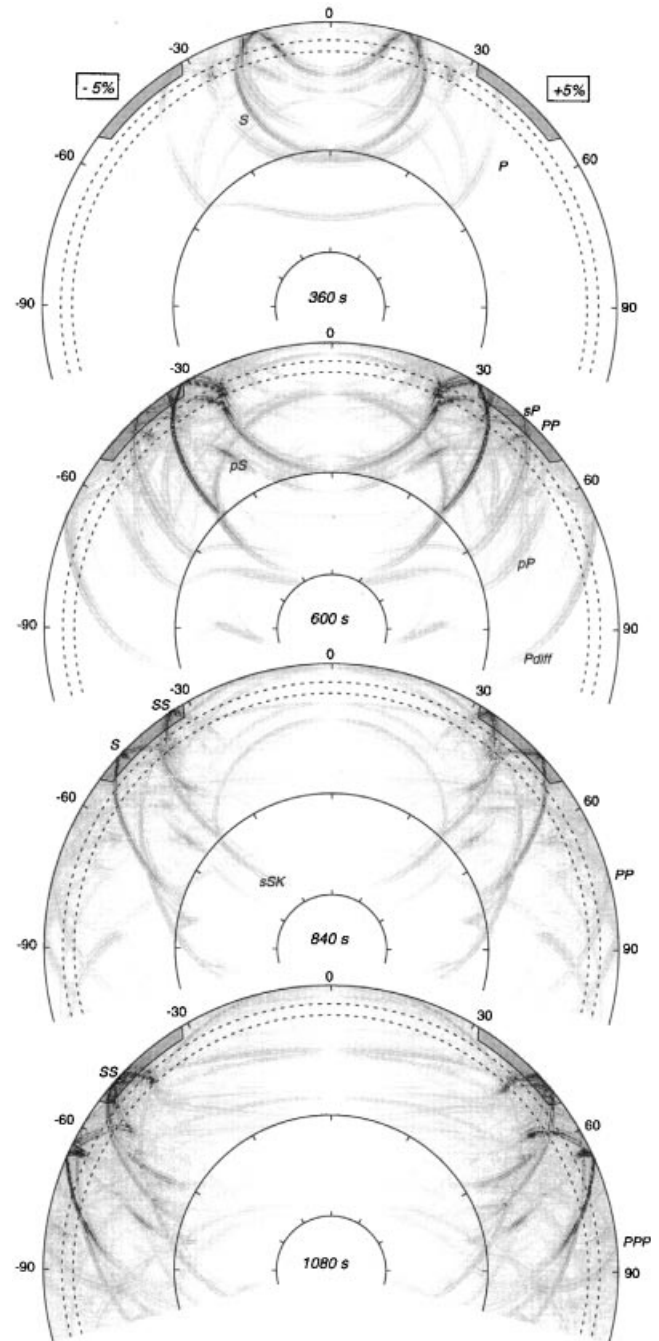


Figure 5. Snapshots of seismic waves propagating in a spherically heterogeneous earth model, with -5 per cent (left) and $+5$ per cent (right) material anomalies just below the free surface (dark zone). The wavefield is displayed for the epicentral distance range -105° to 105° . The contribution of the *P* wave is shown in grey and the *S* wave is shown in black. Major phases are marked in the figure.

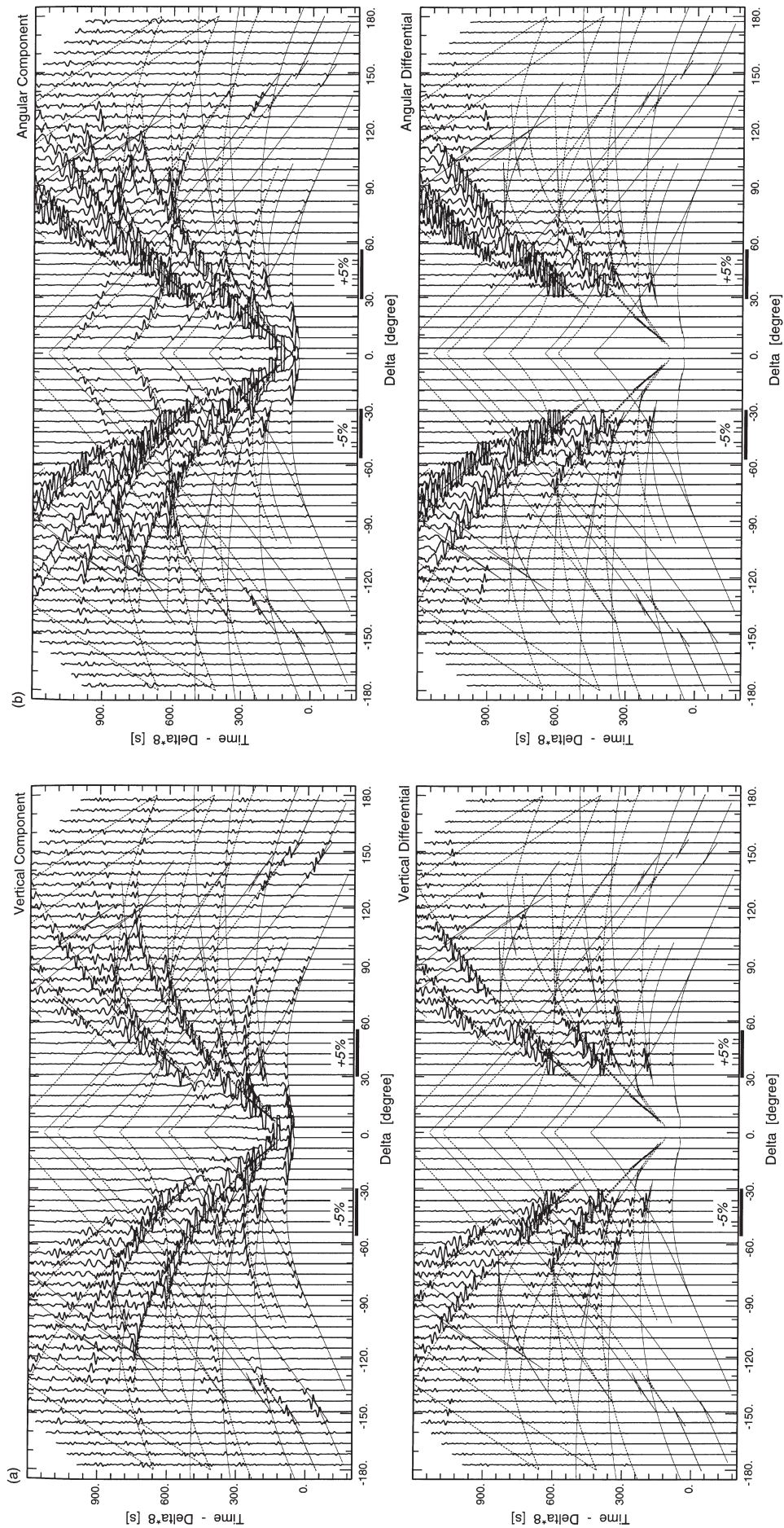


Figure 6. Synthetic velocity seismograms for the spherically heterogeneous earth model with a shield/basin structure of +5 per cent (left) and -5 per cent (right) material anomaly (dark line zone) and differential seismograms denoting relative change in the seismograms from the homogeneous whole earth model. (a) Synthetic seismograms for vertical (r) component and (b) angular (θ) component. Differential seismograms for each component are displayed at the bottom of each record section.

& van der Hilst 1996) in order to enhance the visibility of seismic disturbances in the zone. This higher-wave-speed model is balanced by an equivalent negative anomaly with a -5 per cent perturbation that is the same size as the shield, which is placed on the opposite side from the source. We have used the same source mechanism and depth as in the previous experiment so we can make direct comparisons with the snapshots and synthetic seismograms of the previous reference model.

Fig. 5 displays snapshots of the seismic wavefield for this model with shallow heterogeneity using a regular time interval between frames and the same amplification factor for each frame.

In the first (360 s) frame we see the P wave propagating into the regions of raised and lowered velocities with an advanced or retarded wave front. At 600 s pP , PP and sP phases propagate through the anomalous zones. These phases have acquired a larger amplitude in the case of reduced wave speed on the left than in the higher wave speed (shield) on the right. In the 840 s frame the S -wave front has reached the perturbed regions. On the left, the lowered-wave-speed feature has produced a pronounced S -to- P conversion at the edge so that a large Rayleigh wave is produced from the coupling between the P wave and the SV waves. However, for the higher-wave-speed zone on the right the surface wave is much weaker because the S -to- P conversion is not so strong.

At 1080 s the SS phase is about to leave the lowered-wave-speed zone, on the left, followed by a large and long wave train. The SS and SSS phases propagating through the region are weakened by the increased attenuation as well as energy conversion to a P wave.

Synthetic seismograms for the vertical and angular velocity components at the surface stations are illustrated in Fig. 6. Superposed on the seismograms are the traveltimes for P and S for the reference earth model from Fig. 3. In the lower panel of each of the seismogram displays we show differential seismograms displaying the differences between the results for the heterogeneous model and the seismograms for the spherically symmetric reference model from Fig. 3. Such differential seismograms are very sensitive to small changes in arrival time and wave amplitude and so highlight the influence of the heterogeneous features. We also show an expanded seismogram of the vertical and angular components at an epicentral distance range of 30° to 90° in which the change in the waveform affected by the upper-mantle heterogeneities is clearly seen (Fig. 7).

We recall that the two anomalies are placed below the surface at a distance of $\pm 30^\circ$ to $\pm 55^\circ$ from the epicentre. In the synthetic seismograms we can discern delay and advance of the P and S waves due to the varying velocity anomalies below the stations. In the region of the negative anomaly the seismic records are slightly amplified; this is noticeable in the S and SS phases. For stations on the left, outside the anomalous region, S and SS are weakened because of the removal of S -wave energy at the edge through S -to- P conversions. Traveltimes anomalies also occur in the PP and PPP multiples because they penetrate the anomalous regions two and three times. A corresponding change in the wave shape is developed in the S -wave multiples such as SS and SSS . Most core phases are not noticeably affected by this upper-mantle heterogeneity, except for $sSKS$ and $pSKS$ phases, which are produced from surface reflections from the anomalous zone.

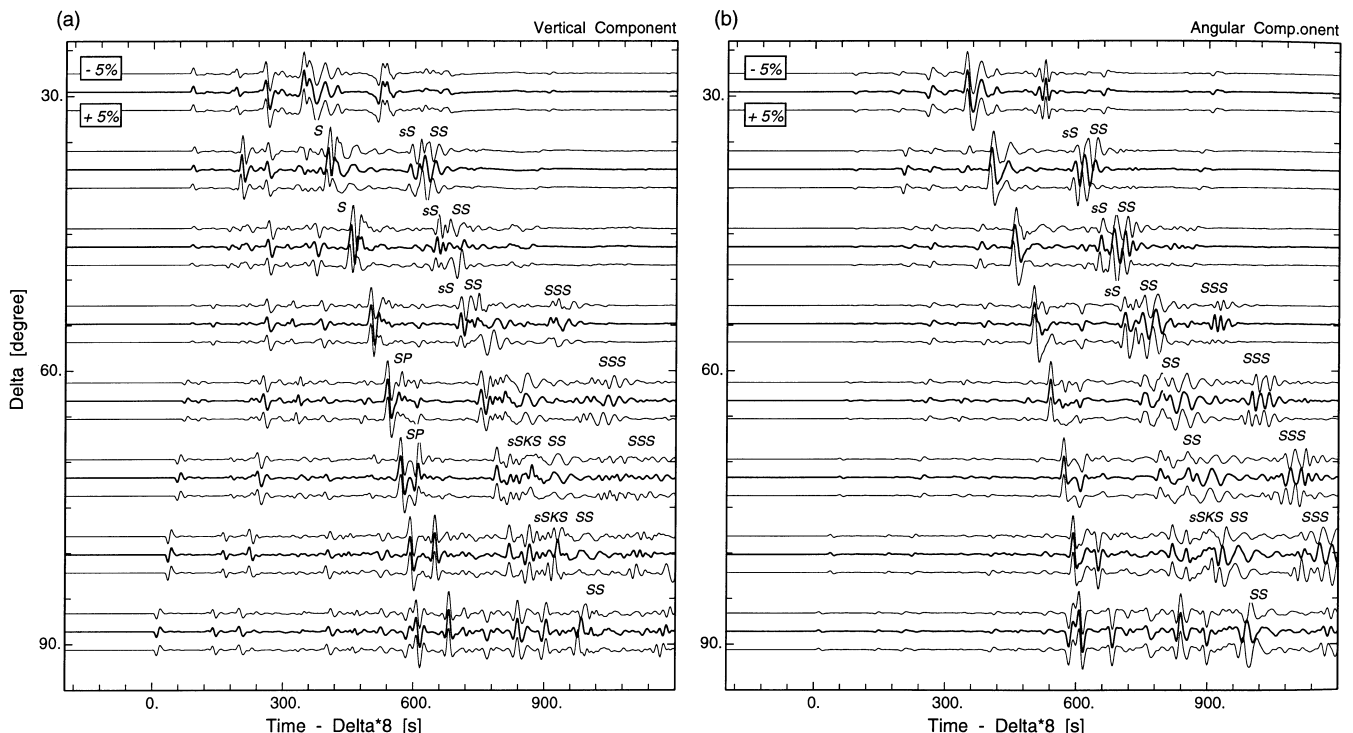


Figure 7. Expanded waveform of Fig. 6 within an epicentral distance range of $\pm 30^\circ$ to $\pm 90^\circ$ demonstrating the change in the wave shape affected by the basin/shield upper-mantle anomalies. At each location three seismograms are presented: for the -5 per cent anomaly (upper trace), the spherically homogeneous model (central thick line) and the $+5$ per cent anomaly (lower trace). (a) Vertical component and (b) angular component. Note that the polarity of the vertical waveform for the left side of the zone (-30° to -90°) is reversed. Major phases are marked.

The example of near-surface heterogeneity demonstrates the way in which large-scale deviations from a spherically averaged structure can have a significant influence on the character of the wavefield both directly through local influences on arrivals and indirectly by the modification of surface multiples that carry the effects to greater distances.

3.3 Example 3: lowermost mantle heterogeneity

Our third example introduces strong deviations from the spherically symmetric reference model in the lowermost mantle just above the CMB. The heterogeneous model consists of two semi-elliptical perturbations (± 5 per cent in material properties) 1600 km wide and 400 km thick placed on top of the CMB in the distance range $\pm 30^\circ$ to $\pm 60^\circ$ from the epicentre (Fig. 8). The scale and level of these anomalies are again about twice as large as suggested from observations (see e.g. Loper & Lay 1995) in order to enhance the visibility of the interaction of seismic phases with the anomalous structures. We use the same source as the previous experiments, so that direct comparisons between snapshot and synthetic seismograms are practicable.

In the first frame (360 s) of Fig. 8 we see the interaction of the P -wave fronts with the abnormal D'' structures. Depending on the sign of the velocity heterogeneity, the wave fronts are slightly advanced/delayed within the zone. It is interesting to note that the P wave penetrating the low-velocity zone over the CMB is strongly bent towards the horizontal so that large P_{diff} and pP_{diff} phases are produced. Consequently, a large P arrival should be observed at distances beyond 100° from the epicentre (see the 600 s frame).

It is also interesting to see that the large pS phase impinging on the higher-velocity-anomaly zone is strongly reflected towards the free surface (see the 840 and 1080 s frames), which should lead to a significant pS arrival at the free surface. However, the pS phase propagating through the lower-velocity anomaly zone is considerably weakened in the high-attenuation material in the zone and so should not readily be seen at surface stations.

Since the S -wave speed for the higher-velocity anomaly is almost as fast as the SK -phase propagation in the core, the triplication in the S -wave group does not appear clearly, whereas, with lowered wave speeds, there is a strong velocity contrast between SK -phase propagation in the core and the S wave in the anomaly zone and in consequence the S -wave triplication is much clearer on the left-hand sides of the snapshots (840 and 1080 s).

Record sections of vertical and angular component synthetic velocity seismograms for this model and the corresponding differential seismograms from the reference case are displayed in Figs 9 and 10. As expected, there is an enhancement of the P_{diff} arrival for epicentral distances beyond -100° on the left due to the influence of the low-velocity inclusion above the CMB. The pP_{diff} arrival is also enhanced. The effects of the different types of anomalies are clearly seen in the differential seismograms with a large discrepancy between the seismograms for the heterogeneous model and the reference model around the S triplication at a distance of about $\pm 80^\circ$ and the sS triplication near $\pm 84^\circ$ in both the vertical and the angular components. The sP phase propagated through the higher-anomaly zone and strongly bent towards the free surface is found at an unusual distance of around 90° from the epicentre.

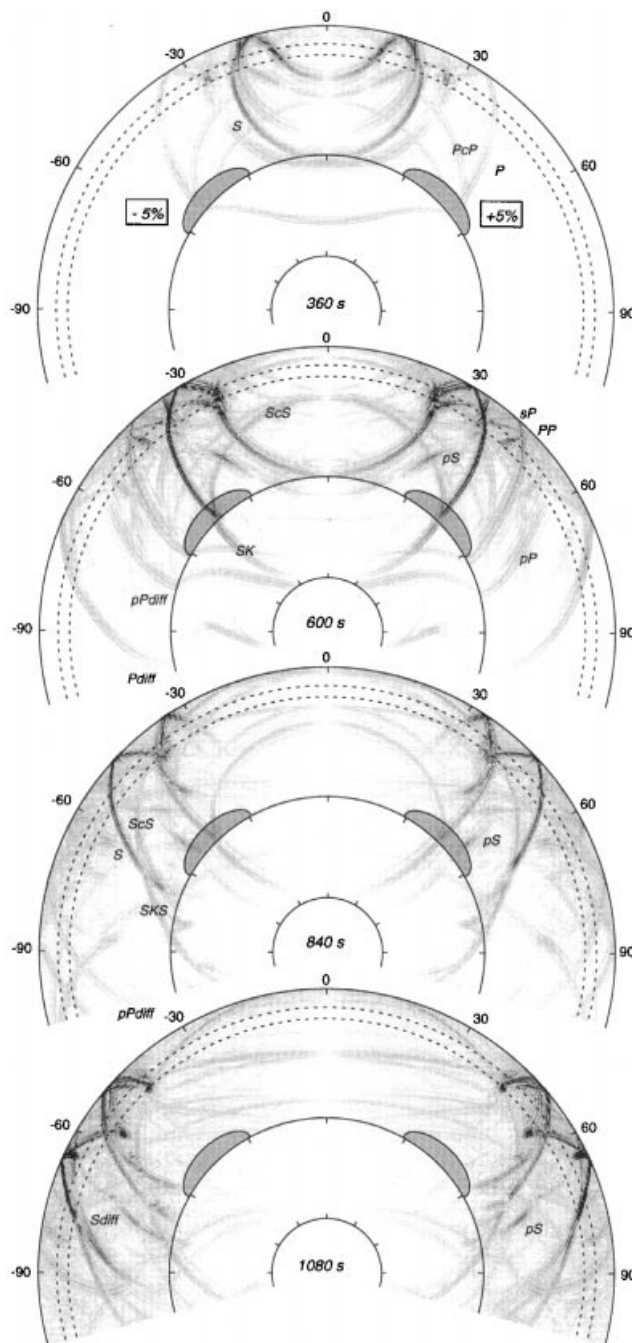


Figure 8. Snapshots of seismic waves propagating in a spherically heterogeneous earth model, with a -5 per cent (left) and a $+5$ per cent (right) anomaly just above the CMB (dark zone). The wavefield is displayed for the epicentral distance range -105° to 105° . Major phases are marked.

Traveltime anomalies are seen in the pP phase around a distance of $\pm 90^\circ$ from the epicentre, and also in the PcP and $PKiKP$ phases near $\pm 60^\circ$, which are produced from the P wave propagating through the anomalies.

Evidence is increasing for widespread and complex heterogeneity in the zone above the CMB including anisotropic effects (see e.g. Loper & Lay 1995). This simple illustration demonstrates the way in which such structure can have a significant influence on parts of the wavefield, including

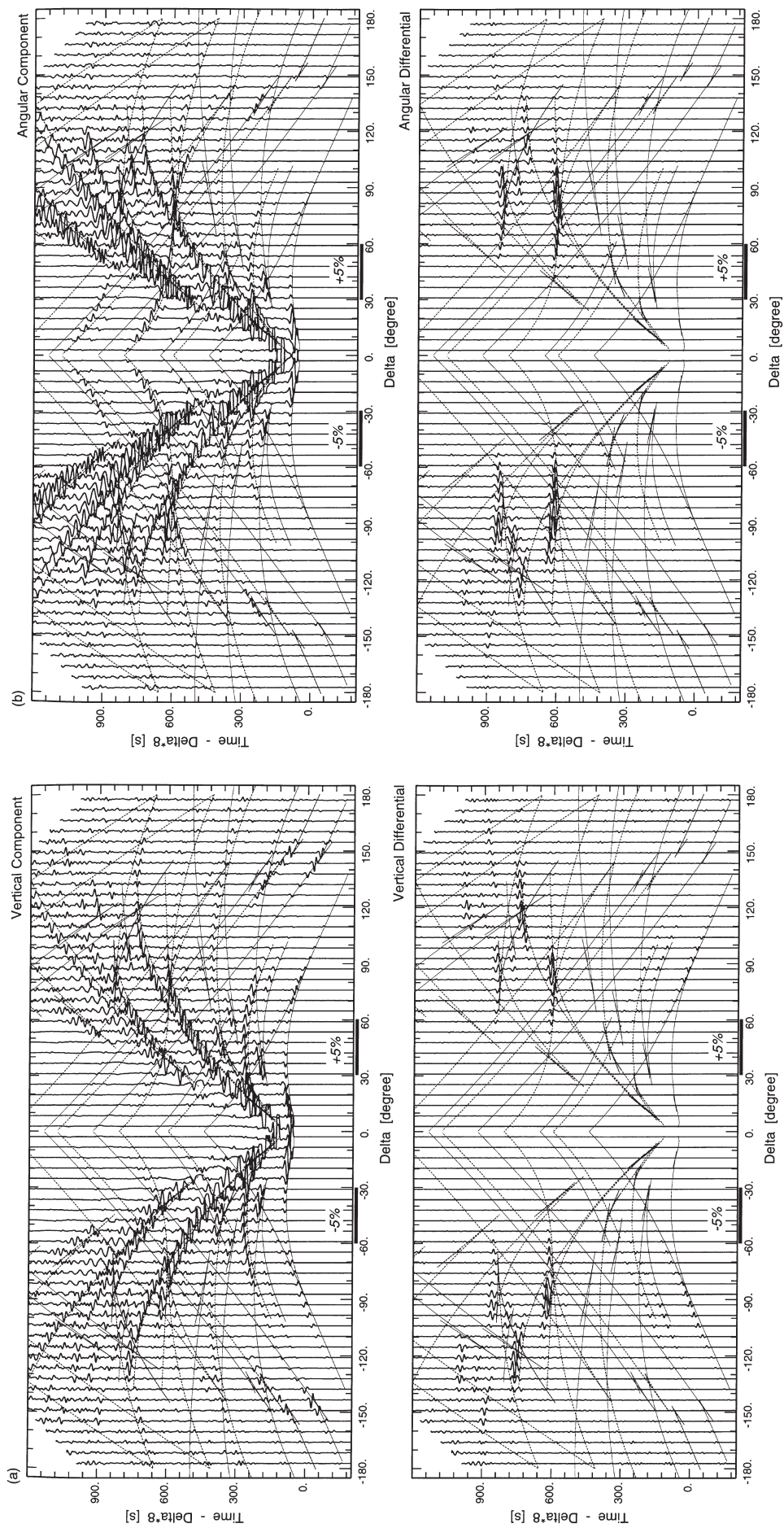


Figure 9. Synthetic velocity seismograms for the spherically heterogeneous earth model with anomalies over the CMB marked by the dark lines. Synthetic seismograms for (a) the vertical (v) component and (b) the angular (θ) component. Differential seismograms for each component are displayed in the bottom panel of each record section.

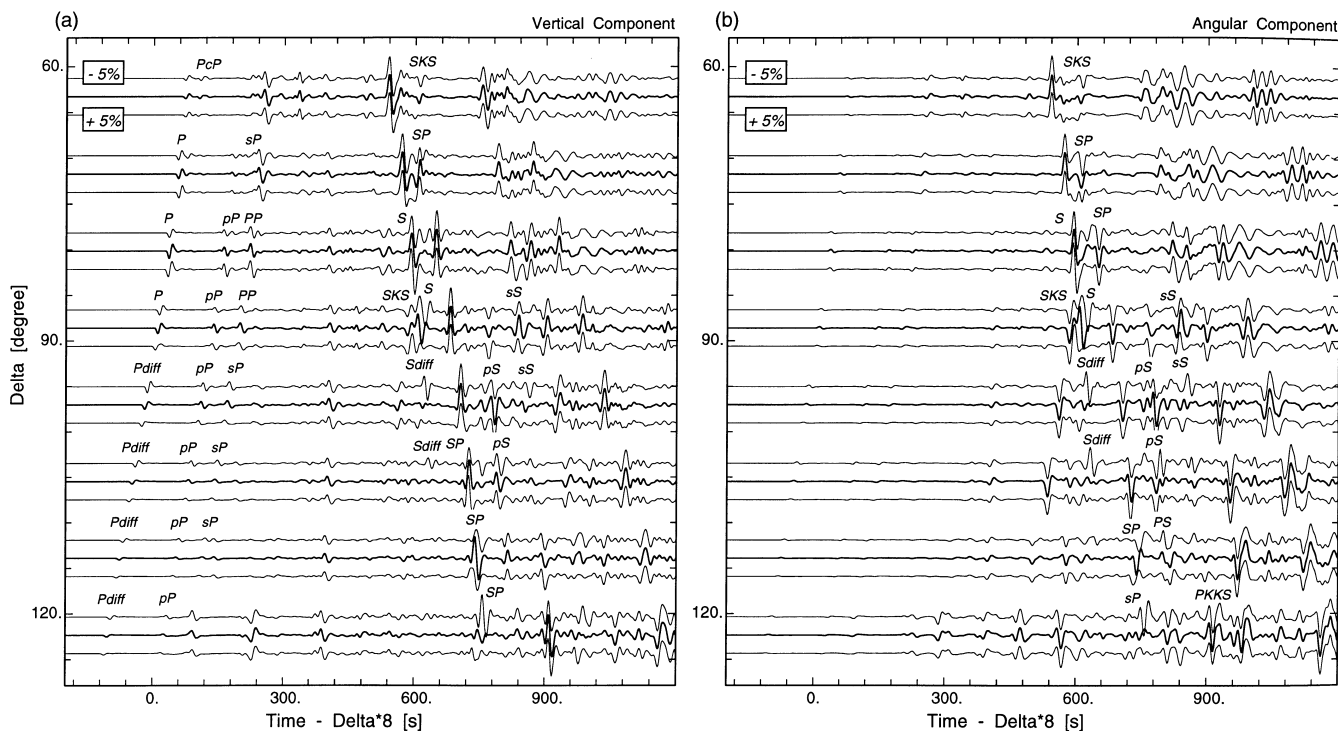


Figure 10. Expanded waveform of Fig. 9 within an epicentral distance range of $\pm 60^\circ$ to $\pm 120^\circ$ demonstrating the change in the wave shape due to the CMB anomalies. At each location three seismograms are presented for the -5 per cent anomaly (upper trace), the spherically homogeneous model (central thick line) and the $+5$ per cent anomaly (lower trace). (a) Vertical component and (b) angular component. Note that the wave amplitude at the left side of the zone (-60° to -120°) is reversed.

enhancing the visibility of phases that would generally have low amplitude (e.g. P_{diff}). The details of deep heterogeneity will frequently be reflected in subtle variations in the character of seismic phases that can get further distorted by near-surface effects, as seen in the previous example.

4 DISCUSSION AND CONCLUSIONS

We have presented the PSM method for simulating a 2-D approximation to seismic wave propagation in a laterally heterogeneous 2-D earth model. Since no numerical dispersion error arises from the accurate differentiation scheme used in the PSM simulation, it is very suitable for large-scale simulation of seismic waves in strongly heterogeneous whole earth models.

We have demonstrated the effectiveness of the calculation procedure using a set of 2-D simulations of seismic waves propagating in a spherically homogeneous earth as well as a strongly heterogeneous earth model. With the aid of a sequence of snapshots of seismic waves separated into P - and SV -wave contributions supplemented by synthetic seismograms, one can clearly see the nature of the seismic wavefield within the earth. Differential seismograms that compare the change in character of seismic phases from that expected for a homogeneous reference earth model provide a useful tool for examining the influence of heterogeneous structure in the mantle.

The restriction to a 2-D implementation in a cylindrical coordinate system for the PSM method arises from the

limitations of current computer power. The simulations are useful for examining the effect of many types of heterogeneity but care should be taken when comparing the synthetic seismograms with any observations, since the geometrical spreading of the line sources implicitly assumed in the 2-D modelling is somewhat smaller than the actual wavefield from a 3-D point source, and moreover scattering and focusing/defocusing effects from out-of-plane wavefields are implicitly neglected in the 2-D modelling.

The computational requirements for the 2-D simulations with a source function with dominant period of 15 s presented here are 85 Mbyte memory in a single precision calculation with a CPU time of 115 hours on a DEC Alpha workstation (500 MHz clock speed) in order to evaluate seismic wave propagation to an elapsed time of 2600 s. Extension of the PSM method to 3-D modelling, the final goal of our simulation study, is relatively straightforward, and we have already prepared the 3-D code with the knowledge obtained from the current simulations. However, full 3-D simulation is still very expensive, even using the PSM. For example, the computer power required for a 3-D hemisphere earth model simulation with the same grid size as the 2-D simulation requires about 1 TByte memory and a computation time of 14 000 hours, and so is practically unrealistic. However, we believe that the trend of steadily increasing computer power and parallel-computing algorithms (e.g. Reshef *et al.* 1988; Liao & McMechan 1993; Furumura *et al.* 1998) will bring closer the use of full 3-D spherical earth simulations for practical applications even at relatively short periods.

ACKNOWLEDGMENTS

The authors are very grateful to Phil Cummins, Japan Marine Science & Technology Center, for making available the DSM program package that was used for computing synthetic seismograms in the spherical earth model. TF would like to acknowledge support from the Japanese Ministry of Education for research abroad and the Research School of Earth Sciences, the Australian National University. This work was undertaken whilst TF was a Visiting Fellow at the RSES, ANU. The authors gratefully acknowledge the constructive reviews by W. Friederich and an anonymous reviewer.

REFERENCES

- Aki, K. & Richards, P.G., 1980. *Quantitative Seismology: Theory and Methods*, Vol. I, W. H. Freeman, San Francisco.
- Alterman, Z.S., Aboudi, J. & Karal, F.C., 1970. Pulse propagation in a laterally heterogeneous solid elastic sphere, *Geophys. J. R. astr. Soc.*, **21**, 243–260.
- Cerjan, C., Kosloff, D., Kosloff, R. & Reshef, M., 1985. A non-reflecting boundary condition for discrete acoustic and elastic wave equations, *Geophysics*, **50**, 705–708.
- Chaljub, E. & Tarantola, A., 1997. Sensitivity of SS precursors to topography of the upper-mantle 660-km discontinuity, *Geophys. Res. Lett.*, **24**, 2613–2616.
- Cummins, P.R., Geller, R.J., Hatori, T. & Takeuchi, N., 1994a. DSM complete synthetic seismograms: SH, spherically symmetric case, *Geophys. Res. Lett.*, **21**, 533–536.
- Cummins, P.R., Geller, R.J. & Takeuchi, N., 1994b. DSM complete synthetic seismogram: P-SV, spherically symmetric case, *Geophys. Res. Lett.*, **21**, 1663–1666.
- Cummins, P.R., Takeuchi, N. & Geller, R.J., 1997. Computation of complete synthetic seismograms for laterally heterogeneous models using the Direct Solution Method, *Geophys. J. Int.*, **130**, 1–16.
- Daudt, C.R., Braile, L.W., Nowack, R.L. & Chiang, C.S., 1989. A comparison of finite-difference and Fourier method calculations of synthetic seismogram, *Bull. seism. Soc. Am.*, **79**, 1210–1230.
- Dziewonski, A.M. & Anderson, D.L., 1981. Preliminary reference earth model, *Phys. Earth planet. Inter.*, **25**, 297–356.
- Fornberg, B., 1987. The pseudospectral method: comparisons with finite-differences for the elastic wave equations, *Geophysics*, **52**, 483–501.
- Fornberg, B., 1988. The pseudospectral method: accurate representation of interfaces in elastic wave calculations, *Geophysics*, **53**, 625–637.
- Friederich, W. & Dalkolmo, J., 1995. Complete synthetic seismogram for a spherically symmetric earth by a numerical computation of the Green's function in the frequency domain, *Geophys. J. Int.*, **122**, 537–550.
- Fung, Y.C., 1965. *Foundations of Solid Mechanics*, Prentice Hall, New York.
- Furumura, T. & Takenaka, H., 1992. A stable method for numerical differentiation of data with discontinuities at end-points by means of Fourier transform-symmetric differentiation, *Butsuri-Tansa (J. SEGJ)*, **45**, 303–309 (in Japanese with English abstract).
- Furumura, T. & Takenaka, H., 1996. 2.5-D modeling of elastic waves using the pseudospectral method, *Geophys. J. Int.*, **124**, 820–832.
- Furumura, T., Kennett, B.L.N. & Takenaka, H., 1998. Parallel 3-D pseudospectral simulation of seismic wave propagation, *Geophysics*, **63**, 279–288.
- Geller, R.J., Ohminato, T., 1994. Computation of synthetic seismograms and their partial derivatives for heterogeneous media with arbitrary natural boundary conditions using the Direct Solution Method (DSM), *Geophys. J. Int.*, **116**, 421–446.
- Graves, R.W., 1996. Simulating seismic wave propagation in 3D elastic media using staggered-grid finite differences, *Bull. seism. Soc. Am.*, **86**, 1091–1106.
- Herrmann, R.B., 1979. SH-wave generation by dislocation source—a numerical study, *Bull. seism. Soc. Am.*, **69**, 1–15.
- Igel, H. & Gudmundsson, O., 1997. Frequency dependent effects on travel times and waveforms of long period S and SS waves, *Phys. Earth planet. Inter.*, **104**, 229–246.
- Igel, H. & Weber, M., 1995. SH-wave propagation in the whole mantle using high-order finite differences, *Geophys. Res. Lett.*, **22**, 731–734.
- Igel, H. & Weber, M., 1996. P-SV wave propagation in Earth's mantle using finite differences: application to heterogeneous lowermost mantle structure, *Geophys. Res. Lett.*, **23**, 415–418.
- Kang, I.B. & McMechan, G.A., 1990. Two-dimensional elastic pseudospectral modeling of wide-aperture seismic array data with application to the Wichita Uplift–Anadarko Basin region of southwestern Oklahoma, *Bull. seism. Soc. Am.*, **80**, 1677–1695.
- Kennett, B.L.N. & Engdahl, E.R., 1991. Traveltimes for global earthquake location and phase identification, *Geophys. J. Int.*, **105**, 429–465.
- Kessler, D. & Kosloff, D., 1990. Acoustic wave propagation in 2-D cylindrical coordinates, *Geophys. J. Int.*, **103**, 577–587.
- Kessler, D. & Kosloff, D., 1991. Elastic wave propagation using cylindrical coordinates, *Geophysics*, **56**, 2080–2089.
- Kosloff, D., Reshef, M. & Loewenthal, D., 1984. Elastic wave calculation by the Fourier method, *Bull. seism. Soc. Am.*, **74**, 875–891.
- Kosloff, D., Kessler, D., Filho, A.Q., Tessmer, E., Behle, A. & Strahilevitz, R., 1990. Solution of the equations of dynamic elasticity by a Chebyshev spectral method, *Geophysics*, **55**, 734–748.
- Liao, Q. & McMechan, G.A., 1993. 2-D pseudospectral viscoacoustic modeling in a distributed-memory multiprocessor computer, *Bull. seism. Soc. Am.*, **83**, 1345–1354.
- Loper, D.E. & Lay, T., 1995. The core-mantle boundary region, *J. geophys. Res.*, **100**, 6397–6420.
- Nielsen, P., If, F., Berg, P. & Skovhgaard, O., 1994. Using the pseudospectral technique on curved grids for 2D acoustic forward modelling, *Geophys. Prospect.*, **42**, 321–341.
- Reshef, M., Kosloff, D., Edwards, M. & Hsiung, C., 1988. Three-dimensional elastic modeling by the Fourier Method, *Geophysics*, **53**, 1184–1193.
- Song, Z.-M. & Williamson, P.R., 1995. Frequency-domain acoustic-wave modeling and inversion of crosshole data: Part I—2.5-D modeling method, *Geophysics*, **60**, 788–795.
- Tal-Ezer, H., Carcione, J.M. & Kosloff, D., 1990. An accurate and efficient scheme for wave propagation in linear viscoelastic media, *Geophysics*, **55**, 1366–1379.
- Tessmer, E., Kosloff, D. & Behle, A., 1992. Elastic wave propagation simulation in the presence of surface topography, *Geophys. J. Int.*, **108**, 621–632.
- Vidale, J.E., 1990. Comments on 'A comparison of finite-difference and Fourier method calculations of synthetic seismograms by C.R. Daudt et al.' *Bull. seism. Soc. Am.*, **80**, 493–495.
- Vidale, J.E., Helmberger, V. & Clayton, R.W., 1985. Finite-difference seismograms for SH waves, *Bull. seism. Soc. Am.*, **75**, 1765–1782.
- Wyssession, M.E. & Shore, P.J., 1994. Visualization of whole mantle propagation of seismic shear energy using normal mode summation, *Pure appl. Geophys.*, **142**, 295–310.
- Yoon, K.-H. & McMechan, G.A., 1995. Simulation of long-period 3-D elastic responses for whole earth models, *Geophys. J. Int.*, **120**, 721–730.
- Zielhuis, A. & van der Hilst, R.D., 1996. Upper-mantle shear velocity beneath eastern Australia from inversion of waveforms from SKIPPY portable arrays, *Geophys. J. Int.*, **127**, 1–16.